UCLA
UCLA Previously Published Works

Title

Hydrologic cycle weakening in hothouse climates.

Permalink

https://escholarship.org/uc/item/8pj0825h

Journal

Science Advances, 10(17)

Authors

Liu, Jiachen

Yang, Jun

Ding, Feng

et al.

Publication Date

2024-04-26

DOI

10.1126/sciadv.ado2515

Peer reviewed

ATMOSPHERIC SCIENCE

Hydrologic cycle weakening in hothouse climates

Jiachen Liu[1], Jun Yang[1]*, Feng Ding[1], Gang Chen[2], Yongyun Hu[1]

The hydrologic cycle has wide impacts on the ocean salinity and circulation, carbon and nitrogen cycles, and the ecosystem. Under anthropogenic global warming, previous studies showed that the intensification of the hydrologic cycle is a robust feature. Whether this trend persists in hothouse climates, however, is unknown. Here, we show in climate models that mean precipitation first increases with rising surface temperature, but the precipitation trend reverses when the surface is hotter than ~320 to 330 kelvin. This nonmonotonic phenomenon is robust to the cause of warming, convection scheme, ocean dynamics, atmospheric mass, planetary rotation, gravity, and stellar spectrum. The weakening occurs because of the existence of an upper limitation of outgoing longwave emission and the continuously increasing shortwave absorption by H_2O and is consistent with atmospheric dynamics featuring the strong increase of atmospheric stratification and marked reduction of convective mass flux. These results have wide implications for the climate evolutions of Earth, Venus, and potentially habitable exoplanets.

INTRODUCTION

In the study of climate change, one of the key findings is that global-mean precipitation (P_m) should increase with surface temperature (T_s), which is supported by numerous climate simulations, theoretical derivations, and observations [e.g., (1–4)]. This conclusion was obtained from studies of climates that are relatively close to modern Earth, typically within ±10 K. Whether the conclusion can be applied to much hotter climates is unknown. In our study, we reveal the presence of a critical transition point in the relationship between P_m and T_s. Below this threshold, P_m exhibits an increasing trend with T_s ($dP_m/dT_s > 0$), whereas above it, the trend reverses, featuring a reduction in P_m with T_s ($dP_m/dT_s < 0$). For Earth's atmosphere and orbit, this transition from intensification to weakening occurs at around 320 to 330 K. This suggests that the previously discovered conclusion cannot be generalized to hothouse climates.

Over a long-term average, P_m is determined by surface or atmospheric energetic constraint [e.g., (5–8)]. Quantitatively, outgoing longwave radiation to space (OLR) is balanced by net longwave radiation from the surface (NLW^s), atmospheric shortwave absorption (ASW^a), sensible heat flux from the surface (SH^s), and condensation heating from precipitation ($L\rho_w P_m$), written as

$$L\rho_w P_m = OLR - NLW^s - ASW^a - SH^s \qquad (1)$$

where L is the latent heat of vaporization, ρ_w is the liquid water density, and ($OLR - NLW^s$) is atmospheric net longwave emission. The dominant terms are $L\rho_w P_m$, OLR, NLW^s, and ASW^a, while the term SH^s is smaller. For the modern Earth, the four terms on the right-hand side (RHS) of Eq. 1 are respectively 240 ± 3, 52 ± 9, 75 ± 10, and 24 ± 7 W m^{-2} (9), and the estimated P_m is ~3.09 ± 0.35 mm day^{-1}, close to reanalysis data. Previous studies showed that P_m increases with T_s and the increasing rate is around 2 to 3%/K [e.g., (3, 4)]. The main reason for the intensification of precipitation is the increase of $OLR - NLW^s$ with T_s (10), which is dominated by the decrease of NLW^s (11).

At low temperatures, OLR is an approximately linearly increasing function of T_s (12). At high temperatures, however, OLR asymptotes

to a limiting, maximum value ($dOLR/dT_s = 0$) when the atmosphere becomes optically thick in all infrared wavelengths and only thermal radiation from the upper troposphere can emit to space (13, 14). For instance, the limiting OLR is ~282 W m^{-2} for a pure water vapor atmosphere (15). However, ASW^a should continue to increase with T_s because the atmospheric absorption in shortwave wavelengths has not reached saturation. The shortwave absorption predominately depends on water vapor concentration, which increases exponentially with temperature following the Clausius-Clapeyron relation. These different trends of longwave cooling and shortwave absorption when the surface is warmer than 320 K were depicted in Jeevanjee and Romps (10). Inspired by the insightful work of Jeevanjee and Romps (10), we speculate that P_m would decrease with T_s ($dP_m/dT_s < 0$) when the increasing rate of ASW^a exceeds that of OLR in hothouse climates. Below, we test this hypothesis through a hierarchy of climate model experiments: global three-dimensional (3D) climate simulations using three different atmospheric general circulation models (GCMs), small-domain 3D radiative-convective simulations using two cloud-resolving models, and 1D radiation calculations using a radiative transfer model, as described in table S1 and Materials and Methods.

RESULTS

The trend of mean precipitation

P_m initially increases with T_s and then decreases (Fig. 1). The transition from an increasing to a decreasing trend occurs within a range of ~320 to 330 K. The increasing trend of P_m below the transition temperature is consistent with previous studies (1–4, 16), whereas the decreasing trend beyond the transition temperature (10) is a less-explored phenomenon emphasized in this study. The nonmonotonic relationship between P_m and T_s is found in both global climate simulations with parameterized convection and clouds (Fig. 1, A to C) as well as small-domain cloud-resolving simulations with explicit convection and clouds (Fig. 1D). The trend is independent of the cause of warming due to increasing CO_2 (Fig. 1, B and C), raising solar constant (Fig. 1A), or specifying T_s (Fig. 1D). However, the cause of warming does influence the maximum P_m (ranging 3.5 and 5.5 mm day^{-1}) and the transition temperature. The transition temperature is lower as CO_2 concentration is higher (Fig. 1B), as CO_2 acts to reduce OLR, consequently lowering P_m for a given T_s (Eq. 1).

[1]Laboratory for Climate and Ocean-Atmosphere Studies, Department of Atmospheric and Oceanic Sciences, School of Physics, Peking University, Beijing 100871, China. [2]Department of Atmospheric and Oceanic Sciences, University of California-Los Angeles, Los Angeles, CA 90095, USA.
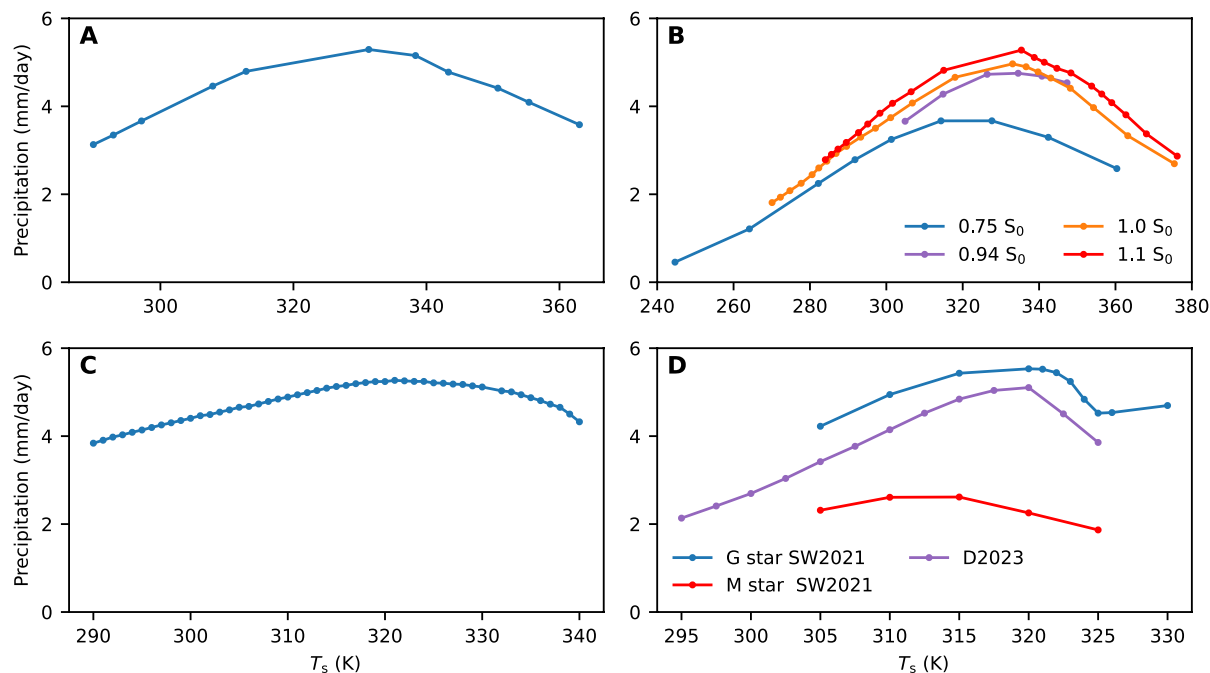*Corresponding author. Email: junyang@pku.edu.cn

Fig. 1. Mean surface precipitation as a function of mean surface temperature (T_s) simulated by three global climate models and by two cloud-resolving models.
(**A**) ExoCAM experiments with increasing solar constant (*18*). (**B**) ExoCAM (*48*) and CAM3 experiments with increasing CO_2 concentration under 0.75 (blue), 0.94 (purple),
1.0 (orange), and 1.1 (red) times modern solar constant (S_0). For a given T_s, the input CO_2 concentration is higher for a lower solar constant. (**C**) ExoCAM experiments with
increasing CO_2 concentration for an aqua-planet with modern solar constant (*49*). (**D**) Small-domain fixed-SST (sea surface temperature) cloud-resolving experiments us-
ing DAM (*22*) and SAM (*45*). Blue and red lines show results with the solar spectrum (blue) and an M star spectrum (red) in (*22*), and the purple line depicts results from (*45*).
Mean precipitation is a nonmonotonic function of T_s and weakens under hothouse climates.

In addition, the nonmonotonic trend is insensitive to land-sea con-
figuration, as the experiments in Fig. 1 (A and B) were conducted
with modern Earth's land-sea configuration or reconstructed Earth's
paleography ~630 million years ago, while the experiments in Fig. 1
(C and D) were coupled with surface ocean everywhere. These re-
sults suggest that the weakening of P_m under hothouse climates
is robust.

On the basis of the surface energy budget, previous studies (*6–8,
17*) suggested that global-mean precipitation is a monotonic function
of surface temperature and asymptotically approaches a maximum
value at ~320 K. Here, we show that the global-mean precipitation is
a nonmonotonic function and decreases with increasing surface tem-
perature in hothouse climates. One reason for the difference is that
previous studies did not explore climates warmer than 320 K. Another
reason is that shortwave absorption was not included in the idealized
gray radiation GCM simulations of O'Gorman and Schneider (*7*),
whereas, in our simulations, both shortwave and longwave radiation
calculations are included. On the basis of analytical argument and
simulation data from a small-domain cloud-resolving model, Jeevanjee
and Romps (*10*) suggested that atmospheric net radiative cooling rate
should decrease with surface temperature when the surface is warmer
than 320 K. Our finding confirms their prediction, explicitly demon-
strating the decreasing trend. Moreover, we extend the phenomenon
to GCMs and apply it to other planets (see the "Applying to other
planets" section), further proving the robustness of this conclusion.

How to understand the nonmonotonic trend of P_m as a function
of T_s? Below, we answer this question through two distinct approaches:
energetic constraint and dynamical constraint, as shown in the
schematic diagram presented in fig. S1.

Mechanisms: Energetic constraint and dynamical constraint
In the context of energetic constraint, energy conservation states
that the amount of atmospheric latent heat release (related to P_m) is
determined by the ability of atmospheric energy loss (Eq. 1). Below
the transition temperature, P_m increases with T_s mainly because
$OLR - NLW^s$ increases with T_s, but the increasing rate becomes
smaller as T_s is close to the transition temperature. Above the transi-
tion temperature, P_m decreases with T_s ($dP_m/dT_s < 0$), because OLR
asymptotes to a constant value when the atmospheric optical thick-
ness becomes large enough (Fig. 2B) and meanwhile atmospheric
shortwave absorption (ASW^a) keeps increasing with T_s (Fig. 2C). The
strong increasing of ASW^a overcomes the change of $OLR - NLW^s$
and other factors. The different trends between longwave and short-
wave are because atmospheric cross sections of water vapor in visi-
ble and near-infrared wavelengths are less than those in thermal
infrared wavelengths [see figure S3 in (*15*)]. As seen in fig. S2B, in
moderate climates, atmospheric absorption in visible and near-
infrared wavelengths is small. As T_s increases, atmospheric emis-
sion reaches saturation at ~320 K in thermal infrared wavelengths,
while the absorption in visible and near-infrared wavelengths keeps
increasing. This energetic constraint is valid in all the experiments
as long as the atmosphere has reached an energy balance (Fig. 2A).

Figure 2 (B and D) suggests that the surface net longwave radia-
tion (NLW^s) and surface sensible heat flux (SH^s) decrease as a func-
tion of T_s. The former indicates that the atmosphere emits more
thermal radiation downward to the surface, because the atmospheric
greenhouse effect increases with T_s, primarily due to the water vapor
feedback. The latter is primarily caused by the diminishing tempera-
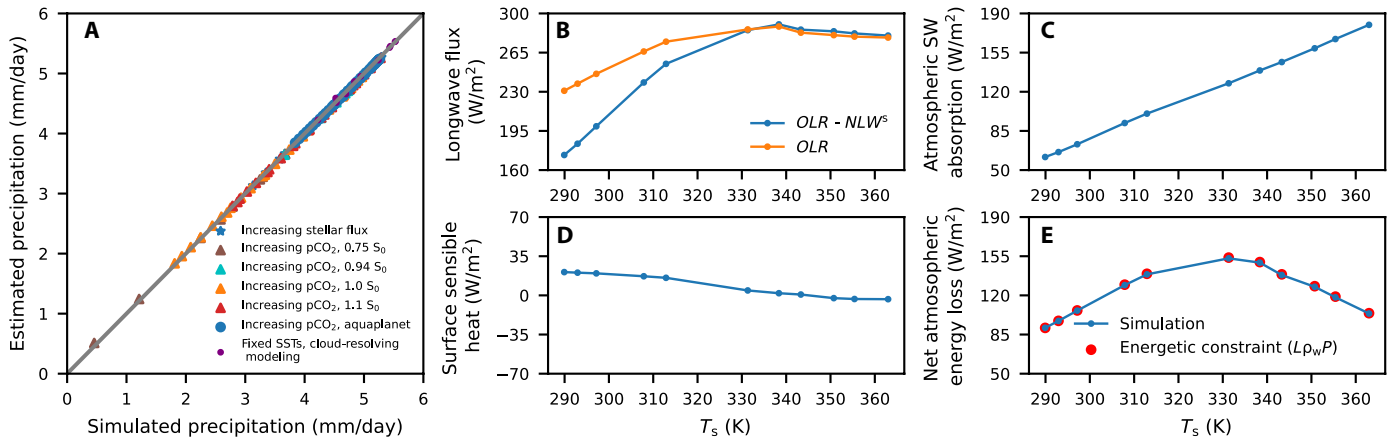ture difference between the surface and near-surface atmosphere as

Fig. 2. Energetic constraint on the mean precipitation. (**A**) Estimated precipitation based on net atmospheric energy loss (divided by $L\rho_w$) versus simulated precipitation in all the experiments. (**B**) Outgoing longwave radiation at the top of the atmosphere (OLR, orange line) and OLR minus net atmospheric thermal emission from the surface ($OLR - NLW^s$, blue line). (**C**) Atmospheric shortwave absorption (ASW^a). (**D**) Surface sensible heat the surface (SH^s). (**E**) Net atmospheric energy loss (blue line, being equal to $OLR - NLW^s - ASW^a - SH^s$) and the estimated latent heat release related to surface precipitation (red dots). Data in (B) to (E) are from Wolf and Toon (*18*). The strength of mean precipitation is constrained by the ability of net atmospheric radiative cooling.

T_s increases. When T_s is higher than ~330 K, NLW^s and SH^s change signs from positive to negative (Fig. 2D), due to the onset of near-surface inversion mainly in the subtropics (*18*). Overall, the change of SH^s is smaller than the other three factors.

In the framework of dynamical constraint, water mass conservation suggests that the surface precipitation in an atmospheric column should be approximately equal to the net water vapor flux entering the column from the cloud base (*2*, *15*, *19*, *20*), expressed as follows

$$P_m \cong \overline{M}\Delta q^* E_p = \overline{M}(q^*_{\text{LCL}} - q^*_{\text{ct}})E_p \qquad (2)$$

in which $\overline{M}$ is the vertically averaged convective mass flux between cloud base and cloud top, q^*_{LCL} is the saturated vapor specific humidity at the lifting condensation level (LCL), q^*_{ct} is the saturated vapor specific humidity at the cloud top, and E_p is the precipitation efficiency (see Materials and Methods). The value of q^*_{ct}, following moist adiabat, is small and negligible in moderate climates but large at hothouse climates. For the cloud-resolving experiments, diagnosed precipitation through Eq. 2 agrees closely with the simulated precipitation with a ~10% difference (Fig. 3A), suggesting that Eq. 2 provides a reasonable estimate to the trend in P_m.

As the surface temperature increases, the P_m trend is mainly determined by the increasing rate of Δq^* and the decreasing rate of $\overline{M}$, while the change in E_p is relatively small across the temperature range (Fig. 3). As T_s increases, Δq^* increases with a rate of about 7%/K following the Clausius-Clapeyron relation (fig. S3B), while $\overline{M}$ decreases. Below the transition temperature (~320 K), Δq^* has larger relative changes than $\overline{M}$, so P_m increases with T_s. However, when T_s surpasses 320 K, $\overline{M}$ is strongly suppressed, exceeding the effect of the increase in Δq^* (fig. S3B), consequently leading to a decrease in P_m with surface warming (fig. S3A). The strong suppression of $\overline{M}$ under warming is mainly caused by the enhancement of atmospheric stratification and the decrease of atmospheric net radiative cooling (*21*–*23*). Therefore, from a dynamical perspective, surface precipitation weakens in hothouse climates primarily because the convective mass flux is markedly suppressed. Note that the argument of the dynamical constraint is not fully independent of the energetic

constraint; for example, the strength of the net radiative cooling is a key factor for determining the magnitude of $\overline{M}$. Nonetheless, it provides dynamic insights on how the atmospheric motion responds to radiation, subsequently affecting convection and precipitation.

In GCMs, precipitation is composed of three parts: deep convective precipitation (P_{deep}), shallow convective precipitation (P_{shallow}), and large-scale precipitation ($P_{\text{large-scale}}$). As the surface warms, P_{deep} first increases and then decreases, P_{shallow} continuously increases with T_s, and $P_{\text{large-scale}}$ monotonically decreases with T_s (fig. S4A). The change of P_{deep} dominates, so the total precipitation changes nonmonotonically with T_s with a transition temperature at ~320 to 330 K. Note that these three types of precipitation are parameterized (*24*) rather than explicitly resolved; therefore, their partitions should be model dependent (*25*). However, the total precipitation should not depend on the parameterization schemes used as it is governed by the energetic constraint shown above.

Above the transition temperature, P_{deep} decreases with T_s because the decreasing rate of deep convective mass flux overweighs the increasing rate of saturation specific humidity (fig. S5, A and B). This mechanism is similar to that found in the cloud-resolving experiments addressed above. The value of P_{shallow} increases monotonically with T_s because the increasing rates of specific humidity and precipitation efficiency outweigh the decreasing rate of shallow convective mass flux (fig. S5, C and D). The tropical Hadley cells and mid-latitudinal synoptic-scale eddies become weaker in a warmer climate (fig. S6), so $P_{\text{large-scale}}$ decreases with T_s.

Zonal-mean precipitation shows that below the transition temperature, precipitation increases in deep tropics and mid-latitudes (fig. S7). Above the transition temperature, precipitation decreases with T_s in the tropics but increases in polar regions. This trend is consistent with the weakening and expansion of tropical circulation and the poleward shift of the mid-latitude baroclinic zone (fig. S6).

Applying to other planets
Besides Earth, our finding is also applicable to other planets, including planets with different stellar spectra (Fig. 1D), slowly rotating planets, and planets with different surface pressures or different
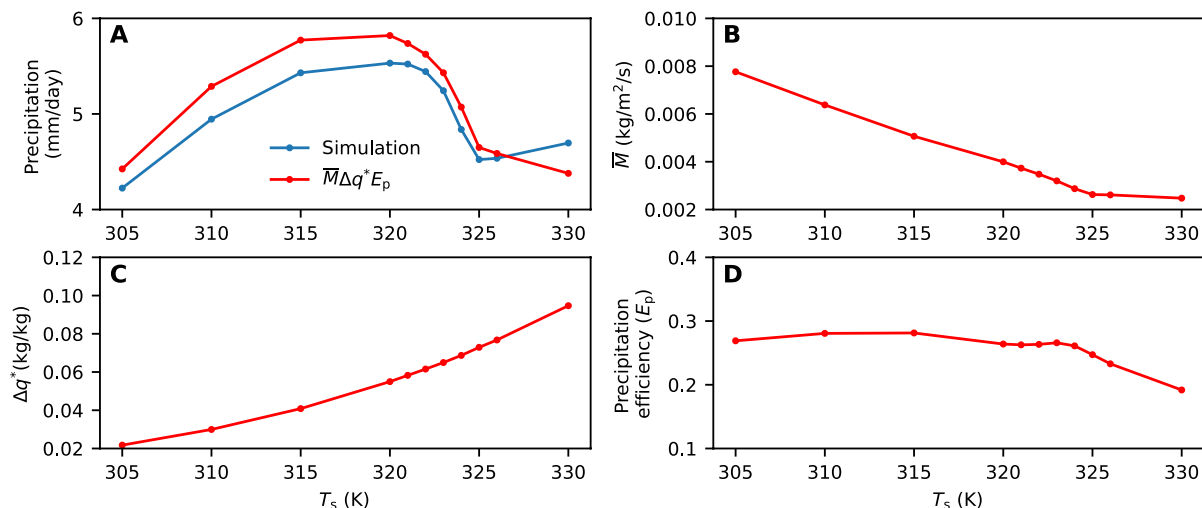
Fig. 3. Dynamical constraint on the mean precipitation. (**A**) Simulated precipitation (blue line) and the estimated precipitation based on Eq. 2 (red line). (**B**) Vertically averaged convective mass flux diagnosed from atmospheric energy balance (Eq. 13 in Materials and Methods). (**C**) Saturated water vapor specific humidity difference between cloud base and cloud top. (**D**) Precipitation efficiency. Data are from the cloud-resolving simulations in Seeley and Wordsworth (*22*). The weakening of the mean precipitation under hothouse climates is mainly due to the reduction in convective mass flux.

gravities (Fig. 4), although the exact values of the maximum precipitation and the transition temperature vary. When changing the stellar spectrum from the Sun to AD Leonis (an M dwarf with an effective temperature of ~3400 K), the maximum precipitation decreases from ~5.5 to 2.5 mm day^{-1}, and the transition temperature changes from ~320 to 310 K. This change is caused by a redder spectrum of AD Leonis and the strong absorption of water vapor and CO_2 in near-infrared wavelengths (0.7 to 5.0 μm). Consequently, more stellar energy is absorbed by the atmosphere rather than the surface (*26*, *27*), resulting in weaker precipitation (refer to Eq. 1) and a lower transition temperature.

For slowly rotating planets, both the maximum precipitation and the transition temperature are lower compared to faster-rotating planets. For example, a planet with a rotation period of 32 Earth days has a maximum precipitation of ~3.5 mm day^{-1} and a transition temperature of ~310 K, while a planet with a rotation period of 256 Earth days has a maximum precipitation of ~2.3 mm day^{-1} and a transition temperature of ~285 K (Fig. 4A). Planetary rotation rate influences the strength of the Coriolis force and the length of day as well as of night. As the rotation period increases, the dayside becomes warmer, leading to a larger diurnal contrast. This enhances night-to-day near-surface convergence, generating more convection during the dayside. Consequently, the dayside water vapor amount and cloud water path increase, resulting in stronger atmospheric shortwave absorption (fig. S8B) and larger planetary albedo (*28*–*30*). In addition, the small differences between Fig. 4 (A and B) suggest that our conclusion is insensitive to ocean dynamics because Fig. 4A is from coupled atmosphere-ocean experiments within which 3D ocean circulation is properly simulated while Fig. 4B is from atmosphere-only experiments where the ocean is immobile.

As surface pressure increases, the transition temperature remains nearly unchanged, while the maximum precipitation decreases moderately (Fig. 4C). This decrease in maximum precipitation is attributed to two factors. First, with larger surface pressure, pressure broadening and collision-induced continuum absorption increase, resulting

in a stronger atmospheric greenhouse effect and a lower *OLR* under a given T_s (fig. S9A). In addition, multiple scattering in the atmosphere increases, leading to larger planetary albedo and meanwhile increased shortwave absorption (ASW^a) by water vapor [fig. S9B and see also (*31*, *32*)]. Both the decreased *OLR* and the increased ASW^a contribute to a weaker precipitation under a higher surface pressure.

As gravity increases, both the maximum precipitation and transition temperature increase (Fig. 4D). This can be explained by two factors. First, a larger-gravity planet has a lower water vapor column mass (although the vapor pressure remains nearly constant under a given surface temperature), resulting in a weaker greenhouse effect and a larger limiting *OLR* which is reached at a higher surface temperature [fig. S9D and see also (*14*, *33*, *34*)]. Second, the dependence of atmospheric shortwave absorption on gravity is tiny (fig. S9E), since a fixed air mass is used in these three experiments.

The precipitation in Fig. 4 (C and D) is derived from 1D radiative transfer modeling and based on the energy conservation analysis (Eq. 1). The weakening precipitation at high temperatures in this simple framework again confirms the robustness of our conclusion.

DISCUSSION
The weakening of precipitation under hothouse climates presents a conceptual advance in our understanding of the climate system of Earth as well as of other rocky planets. Contrary to the previous common view that precipitation constantly increases with rising surface temperature, we demonstrate that the increasing rate of precipitation with surface temperature is state dependent [similar to the climate sensitivity (*35*, *36*)]. Particularly, the increasing rate approaches zero or even becomes negative under hothouse climates.

High surface temperatures limit planetary habitability, and a weakening hydrologic cycle can lead to further challenges for life. For example, the weakening precipitation may shorten the life span
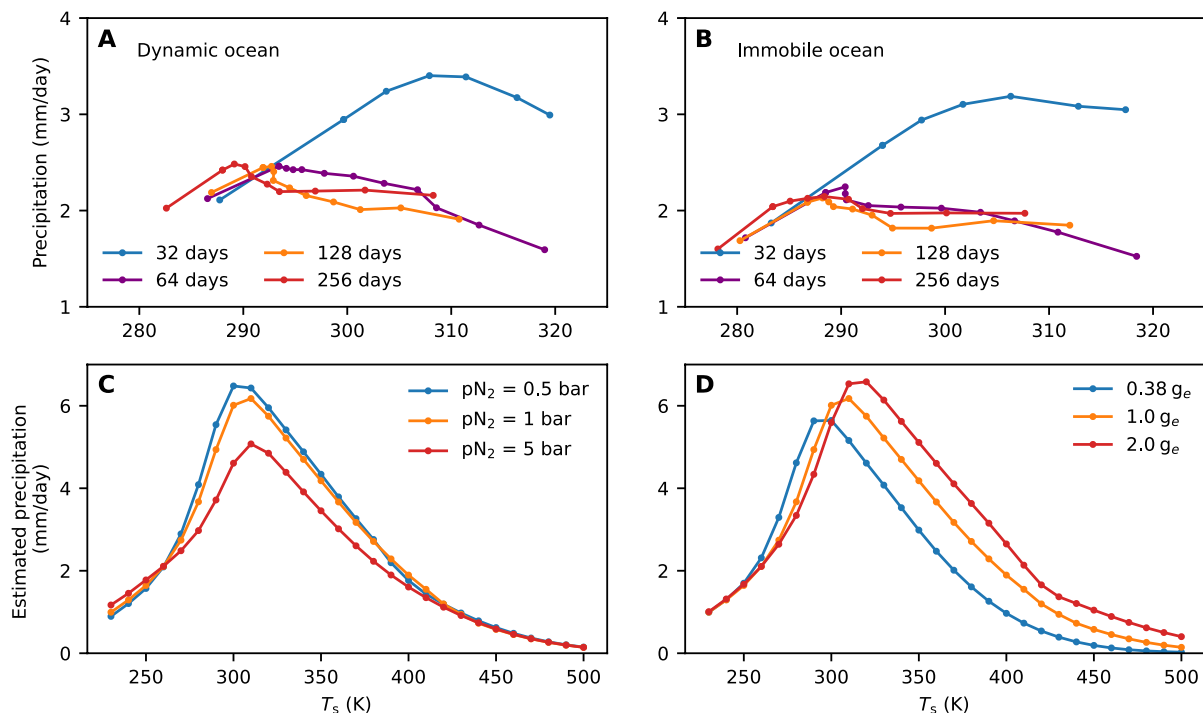
Fig. 4. Mean precipitation under different planetary parameters. (A and **B)** 3D global climate simulations from Way *et al.* (*30*) with planetary rotation periods of 32 (blue), 64 (purple), 128 (orange), and 256 (red) Earth days. The horizontal axis is the global mean surface temperature. The atmosphere is coupled to a dynamic ocean (A) or an immobile ocean (B). (**C** and **D)** Estimated mean precipitation based on 1D atmospheric radiative transfer modeling and atmospheric energetic constraint (see Materials and Methods). (C) Background air pressure is set to 0.5 bar (blue), 1.0 bar (orange), and 5 bar (red) of N_2. (D) Surface gravity is set to 0.38 (blue, Mar's value), 1.0 (orange), and 2.0 (red, corresponding to a super-Earth) times Earth's gravity (9.8 m s^{-2}) with the same air mass (~1 × 10^4 kg m^{-2}). The nonmonotonic trend of mean precipitation with T_s does not depend on rotation periods, ocean dynamics, air pressure, or surface gravity.

of the future Earth's biosphere under the brightening Sun, compared to previous estimations (*37, 38*). This issue should also be pertinent to Early Earth and Mars with a hot surface or a post-impact steam atmosphere, early Venus with a high-level insolation, and exoplanets with large amounts of CO_2/CH_4 or orbiting close to the inner edge of the liquid-water habitable zone (*14, 18, 23, 39, 40*).

Our discovery challenges the fundamental assumption (precipitation increases with surface temperature) used in the hypothesis of the carbonate-silicate cycle (*14, 41*). The weathering rate at high temperatures will be lower than previous anticipation. For instance, in the hothouse climate with high CO_2 levels following the melting of a hard snowball Earth that may have occurred during the Neoproterozoic era in ~600 to 800 million years ago (*42*), the hydrologic cycle strength should be weaker (purple line in Fig. 1B), and the recovery from the postsnowball hot climate should take longer than commonly assumed. Our conclusion confirms and extends previous studies (*6, 17*). Our results also suggest that in a runaway greenhouse state or an extremely hot climate state (>500 K), the surface precipitation will approach zero as shown in Fig. 4 (C and D). Upperlevel convection can still occur, but all day-side precipitating droplets will reevaporate at lower levels before reaching the planetary surface (*23, 43*), similar to the condition observed on modern Venus.

Besides mean precipitation, precipitation variability should also change in hot climates, as suggested in (*22, 44–47*). The temporal pattern of precipitation in hothouse climates may transform from quasi-steady to organized episodic deluges, with outbursts of short and heavy rain alternating with several-day dry spells. Future work

is required to combine these two aspects (mean and variability) of both regional and global precipitation through a unified theoretical framework.

MATERIALS AND METHODS

We use simulation data from three atmospheric GCMs (ExoCAM, ROCKE-3D, and CAM3), two cloud-resolving models: Das Atmosphärische Modell (DAM) and System for Atmospheric Modeling (SAM), and a radiative transfer model (ExoRT) to examine the global-mean or domain-mean precipitation from cold to hot climates. ExoCAM experiments were conducted by Wolf and Toon (*18*), Wolf *et al.* (*48*), and Zhang *et al.* (*49*), ROCKE-3D experiments were performed by Way *et al.* (*30*), DAM experiments were done by Seeley and Wordsworth (*22*), and SAM experiments were performed by Dagan *et al.* (*45*). We use their output data in our analysis. Previous investigations primarily focus on surface temperature and clouds (*18, 30, 48, 49*) or the temporal variability of precipitation (*22, 45*), while our study focuses on the mean precipitation. We conduct experiments using CAM3 and ExoRT (table S1). We use two distinct methodologies to understand the change in globalmean precipitation: energetic constraint and dynamical constraint.

ExoCAM

ExoCAM is a modified version of the Community Earth System Model version 1.2. It uses the Community Atmosphere Model version 4 (*24*), with a horizontal resolution of 4° × 5° and a finite

volume dynamical core. ExoCAM uses a correlated-k two-stream radiative transfer model ExoRT, which is modified to simulate hothouse climates (the hottest air temperature can be up to 500 K) and high-CO_2 atmospheres (50). The deep convection scheme used in ExoCAM is originally from the parameterization developed by Zhang and McFarlane (51) and further modified with the addition of convective momentum transport (52) and dilute entraining plumes (53, 54). The scheme is based on a plume ensemble approach, in which an ensemble of convective scale updrafts occurs once the lower atmosphere is conditionally unstable. The shallow convection scheme is treated by the parameterization of Hack (55), which can be applied to convection rooted in any layers.

For ExoCAM, we use released simulation results of hothouse climates from three published papers: Wolf and Toon (18), Wolf et al. (48), and Zhang et al. (49). Wolf and Toon (18) increased the surface temperature by increasing stellar insolation, while Wolf et al. (48) and Zhang et al. (49) by increasing CO_2 concentration. We use three sets of experimental data from Wolf et al. (48) with different solar constants (0.75, 1.0, and 1.1 times Earth's present-day solar constant, 1360 W m^{-2}). The simulations had all reached equilibrium.

Wolf and Toon (18) and Wolf et al. (48) assumed a 1-bar N_2 background, with the addition of CO_2 and variable H_2O. The total pressure of the atmosphere was the sum of the partial pressures of the three components, N_2, CO_2, and H_2O. Their studies used 45 vertical levels with the model top extending to ~0.2 hPa. Solar spectrum was used. Orbital parameters, such as obliquity, eccentricity, rotation rate, and rotation period, were identical to the present-day Earth. Continental configuration and land coverage were also assumed identical to present-day Earth, except the permanent glacial ice sheets on Antarctica, Greenland, and the Himalayas were replaced by bare soil. A thermodynamic 50-m slab ocean with prescribed internal ocean heat fluxes that mimicked present-day Earth's ocean heat transport was used in their studies. Snow and ice cover were allowed to accumulate once the climates were sufficiently cold.

Zhang et al. (49) assumed a 1-bar N_2 background with variable H_2O. The total pressure of the atmosphere was the sum of the two components, N_2 and H_2O. The CO_2 mixing ratio only affected the radiative transfer scheme and was not included in the total pressure. They used 40 vertical levels with the model top extending to ~1 hPa. Their simulations were conducted with a global ocean surface with no sea ice or continents and with zero ocean heat transport. The stellar insolation (1361 W m^{-2}), the stellar spectrum, and the orbital and rotation periods were identical to present-day Earth's values. Both eccentricity and obliquity were set to zero. We used the simulation results of Group InvCM-ClimateSensitivity in their study. This group of simulations assumed fixed global sea surface temperature with a 1-K increment from 290 to 340 K, and the CO_2 mixing ratio evolved to equilibrate the system.

ROCKE-3D
ROCKE-3D is a generalized version of the Goddard Institute for Space Studies ModelE2. It has been developed to allow large ranges of air temperature, air pressure, rotation rate, and atmospheric composition (56). ROCKE-3D uses a horizontal resolution of 4° × 5° and 20 vertical levels with the model top extending to 0.1 hPa. For ROCKE-3D, we used the released simulation results from Way et al. (30). They used zero obliquity and eccentricity, with land configuration and topography roughly identical to modern Earth. The study assumed a 984-hPa N_2 background, with 400-parts per million by

volume (ppmv) CO_2, 1-ppmv CH_4, and variable H_2O. The effect of variable H_2O on total air mass was neglected. The atmosphere was coupled to two ocean types: a thermodynamic slab ocean with zero lateral ocean heat transport and a fully coupled dynamic ocean with 10 vertical levels down to 1360 m. In our study, we use the simulation results with long rotation periods of 32, 64, 128, and 256 days, which represent the possible climates of slowly rotating planets like Venus.

CAM3
CAM3 (Community Atmosphere Model version 3) is the atmospheric component of the Community Climate System Model version 3 (57, 58). The model is designed to enable a wide range of spectral resolutions. Here, we use the horizontal resolution of 2.8° × 2.8°. We use 26 vertical levels, with the model top reaching 2 hPa. The atmosphere is coupled to a 50-m slab ocean. To simulate the climate of a postsnowball Earth state, the land configuration is set to be the reconstructed global paleogeography of 635 million years ago (59). O_3 concentration is set to half of that on modern Earth, CH_4 is set to 0.806 ppmv, and N_2O is set to 0.277 ppmv. The solar insolation is set to 1284.98 W m^{-2}, 6% lower than the modern Sun. We set the eccentricity to zero, while the obliquity is 23.5°, same as modern Earth. To melt a snowball Earth, CO_2 concentration needs to be very high (60, 61). A series of CO_2 concentrations is tested, 20,000, 40,000, 100,000, 200,000, 300,000, and 400,000 ppmv.

DAM
DAM is a 3D, finite-volume, fully compressible, nonhydrostatic, cloud-resolving model (62). We use the simulation results of hothouse climates from Seeley and Wordsworth (22). All the experiments were nonrotating radiative-equilibrium (RCE) simulations. RCE is an idealization of the tropics as a whole, and it is widely used in studying the essential interactions between convection and radiative transfer. Vertical velocity is explicitly resolved in the model. Water vapor condensation occurs when the air parcel reaches saturation. The microphysics scheme is Lin-Lord-Krueger, which considers six water classes (water, cloud liquid, rain, snow, and graupel). The simulations were conducted on a doubly periodic square domain of 72 km by 72 km, with 140 vertical levels and with free-slip, rigid lids at the top of the model (60 km). The horizontal grid spacings in both directions were 2 km. These grid spacings were high enough to simulate large convective cells such as deep convective plumes and anvil clouds, without using cumulus schemes (63). To obtain more realistic radiative heating rates in hothouse climates, Seeley and Wordsworth (22) coupled DAM to a line-by-line radiation transfer model (64). The diurnal cycle was not included.

Simulation data of both the solar spectrum and an M star spectrum are used in this study. For the solar spectrum experiments, the downward shortwave radiation was 413.13 W m^{-2} at the model top and the solar zenith angle was 43.75°. For the M star spectrum experiments, the downward shortwave radiation was 400 W m^{-2} at the model top, and the solar zenith angle was 48.19°. In the G star experiments of DAM, the radiative effects of clouds are considered, but in the M star experiments, no cloud radiative effect is included. However, this does not influence the nonmonotonic trend of the mean precipitation as shown in Fig. 1D. The simulations had all reached equilibrium, and the final 100 days of the solar spectrum experiments and the final 50 days of the M star experiments are used here.

SAM

SAM is a cloud-resolving model using the anelastic dynamic core, documented by Khairoutdinov and Randall [65]. We use the small-domain RCE simulation results from Dagan *et al.* [45]. The simulations were conducted on a doubly periodic square domain of 96 km by 96 km, with 81 vertical levels extending to 33 km. The horizontal resolution was 1 km. Surface temperatures were prescribed, from 295 to 325 K with 2.5 K intervals. Radiation was calculated using CAM3 radiative scheme [57]. The incoming solar radiation was 551.58 W m^{-2} with a zenith angle of 42.05°. Each simulation was run for 150 days, and the last 50 days were used for the analyses.

Radiative transfer modeling

The 1D radiative transfer model used in this study is ExoRT. ExoRT is a two-stream radiative transfer model. It can be used as either an offline model alone or coupled with 3D climate models such as ExoCAM. The latest version n68equiv uses correlated-k coefficients produced with HELIOS-K [66]. The model uses 68 spectral intervals and 8 gauss points, which can simulate a large range of air temperature (from 100 to 500 K) and air pressure (from 0.00001 to 10 bars).

We do five groups of experiments. In the first three groups, we change the background air pressure (0.5-, 1-, and 5-bar N_2) under fixed surface gravity (Earth's value, 9.8 m s^{-2}). We use 600 vertical levels, with a grid spacing of 400 m. In the other two groups, we change the surface gravity (0.38- and 2-times Earth's gravity) under fixed dry air mass ($\sim 1 \times 10^4$ kg m^{-2}). The lower gravity value is the surface gravity of Mars, and the higher value is approximately the upper gravity limit of super-Earths. We use 1500 and 300 vertical levels for the 0.38- and 2-times Earth's gravity experiments, respectively.

We specify the surface temperature for each group, from 230 to 500 K with 10-K increments. The surface albedo is set to 0.22, considering the effect of clouds and sea ice. The solar constant is set to 680 W m^{-2} with a zenith angle of 60°. The atmosphere is composed of N_2 and H_2O. We assume that the air temperature follows H_2O moist adiabatic profile in the troposphere, and the stratosphere is set to isothermal at 200 K. We consider water vapor to be saturated, with its concentration fixed according to the air temperature profile. The inverse moist adiabatic lapse rate is calculated by

$$\frac{d\ln P}{d\ln T} = \frac{P_n}{P}\frac{d\ln P_n}{d\ln T} + \frac{P_c}{P}\frac{d\ln P_c}{d\ln T} \tag{3}$$

where P_c and P_n are the partial pressures of H_2O and N_2, P is the total pressure, and T is the air temperature. We use the hydrostatic equation to convert the pressure coordinate to the height coordinate. The first term on the RHS of Eq. 3 represents the inverse dry adiabatic lapse rate, which, following Pierrehumbert [14], can be expressed as

$$\frac{d}{d} = \frac{c_{pn}}{R_n} \times \frac{1 + \left[\frac{c_{pc}}{c_{pn}} + \left(\frac{L}{R_c T} - 1\right)\frac{L}{c_{pn} T}\right]\alpha_c}{1 + \frac{L}{R_n T}\alpha_c} \tag{4}$$

Here, c_{pn} and c_{pc} are the specific heat capacities of N_2 and H_2O, R_n and R_c are the specific gas constants of N_2 and H_2O, and α_c is the mass mixing ratio of H_2O. We assume that both N_2 and H_2O behave as ideal gases. The second term on the RHS of Eq. 3 follows the Clausius-Clapeyron relation

$$\frac{d\ln P_c}{d\ln T} = \frac{L}{R_c T} \tag{5}$$

where L is the latent heat vaporization of water vapor. To obtain more precise results, we take into account the dependence of specific heat capacity (c_p) and latent heat of vaporization (L) on air temperature. The specific heat capacity function with respect to temperature can be described by the Shomate Eq. 14

$$c_p = A + B \times \frac{T}{1000} + C \times \left(\frac{T}{1000}\right)^2 + D \times \left(\frac{T}{1000}\right)^3 + E \times \left(\frac{T}{1000}\right)^{-2} \text{J kg}^{-1}\text{K}^{-1} \tag{6}$$

For N_2, this equation is valid from 300 to 500 K, with coefficients A, B, C, D, and E being as 931.857, 293.529, −70.576, 5.688, and 1.587, respectively [14]. Below 300 K, the specific heat capacity of N_2 is set to 1037 J kg^{-1} K^{-1}. For H_2O, this equation is valid from 273 to 1800 K, with coefficients of 161.778, 379.584, 377.413, −140.804, and 4.563, respectively [67]. Below 273 K, the specific heat capacity is set to 1847 J kg^{-1} K^{-1}. The latent heat of vaporization changes with temperature following Kasting [68],

$$\frac{dL}{dT} = c_{pv} - c_w \approx 2230 \text{ J kg}^{-1}\text{K}^{-1} \tag{7}$$

where c_w is the specific heat capacity of liquid water. Thus, L can expressed as $2.5 \times 10^6 - 2230 \times (T - 273.15)$ J kg^{-1}. The saturated water vapor pressure (P_c) is given by experimental data as [69]

$$P_c = \frac{e^{77.3450 + 0.0057T - 7235/T}}{T^{8.2}} \tag{8}$$

The estimated precipitation derived from the 1D radiative transfer modeling (Fig. 4, C and D) is determined by the atmospheric energy constraint, with surface sensible heat flux assumed to be zero (following Eq. 1 with $SH^s = 0$). Clouds are not included in the radiative transfer modeling.

Energetic constraint on precipitation

The energetic constraint is expressed as Eq. 1 and illustrated in fig. S1A. Horizontal and vertical heat and water transports are not explicitly included in the equation. In experiments where the atmosphere is interactively coupled to the surface, both the atmospheric energy budget and the surface energy budget are closed once the experiment has reached equilibrium. In experiments where the surface temperature is fixed, the atmospheric energy budget is closed but not the surface energy budget. In our calculations, we use the atmospheric energy budget to estimate the strength of mean precipitation.

In our analysis, both cloud shortwave and longwave radiative effects are considered unless stated otherwise. Cloud shortwave radiative effect tends to increase planetary albedo thereby reducing shortwave absorption in the atmosphere and at the surface. In addition, cloud particles can absorb near-infrared radiation, leading to a stronger atmospheric shortwave absorption. However, this effect typically has a smaller magnitude compared to water vapor absorption. Consequently, the cloud shortwave radiative effect is not typically the dominant term in the atmospheric energy budget. On the other hand, cloud longwave radiative effect tends to reduce outgoing longwave radiation to space, resulting in a weakening precipitation.

Different GCMs use different parameterization schemes for clouds, so the simulated values in the cloud longwave radiative effect should be model dependent. The cloud-resolving model DAM and SAM can resolve clouds at grid scales of 4 and 1 km^2 respectively, but cloud microphysics (such as cloud particle sizes and cloud droplet falling speeds) still require parameterization. For experiments used in this study, the changes of cloud longwave radiative effect are limited to 10 to 20 W m^{-2}. This limitation is likely due to the nearly constant cloud top temperature (~200 to 220 K), proposed by the fixed anvil temperature hypothesis (70).

Given that an energy of 10 W m^{-2} corresponds to a mean precipitation change of approximately 0.35 mm day^{-1}, such variations are not potent enough to substantially alter the overall trend of precipitation as a function of surface temperature. This suggests that our results are robust to cloud and convection parameterization as shown in Figs. 1 and 4. There is only one exception in our experiments: The blue line in Fig. 1D shows that the mean precipitation at 330 K appears somewhat stronger than that at 325 K. This is primarily attributed to the reduction of the cloud longwave radiative effect from 35.2 W m^{-2} at 325 K to 31.9 W m^{-2} at 330 K.

Dynamical constraint on precipitation in DAM

In the RCE simulations using the cloud-resolving model DAM, the estimation of precipitation can be expressed as Eq. 2. This equation, popularized by Held and Soden (2), has been widely used in numerous studies for diagnosing or analyzing precipitation [e.g., (16, 20, 71)]. We derive Eq. 2 by transforming the original form of Eq. 12 presented in Jeevanjee (20)

$$P_m = E_p \int_{z_{LCL}}^{z_{ct}} \left[-M \frac{dq_v^*}{dz} - \epsilon M (1 - RH) q_v^* \right] dz \quad (9)$$

Here, E_p is the precipitation efficiency, M is the convective mass flux, q_v^* is the saturated water vapor specific humidity, z_{LCL} and z_{ct} are the height of the LCL and cloud top, ϵ is the fractional entrainment per unit distance (m^{-1}), and RH is relative humidity. Romps (72) suggests a characterized RH value of ~75 to 80% in the tropics. For simplicity, we assume that RH is close to one, allowing us to approximate

$$P_m \cong E_p \int_{z_{cb}}^{z_{ct}} -M \frac{dq_v^*}{dz} dz \quad (10)$$

By assuming RH close to one, we neglect the suppression on condensation resulting from the entrainment of drier environmental air into the convective mass. Consequently, this results in an overestimation of mean precipitation. Since M and q_v^* are nearly independent and the change of M with height is relatively small compared to the change of q_v^*, we can express the above equation as

$$P_m \cong -E_p \frac{\sum (M \delta z)}{z_{cb} - z_{ct}} \int_{z_{cb}}^{z_{ct}} \frac{dq_v^*}{dz} dz = E_p \frac{\sum (M \delta z)}{z_{cb} - z_{ct}} (q_{LCL}^* - q_{ct}^*) \quad (11)$$

In this equation, $\frac{\sum M \delta z}{z_{cb} - z_{ct}}$ represents the vertically average convective mass flux, which accounts for the effects of entrainment and detrainment. By using a more concise term $\overline{M}$ to replace $\frac{\sum M \delta z}{z_{cb} - z_{ct}}$, the equation can be rewritten as Eq. 2: $P \cong \overline{M} \Delta q^* E_p = \overline{M} (q_{LCL}^* - q_{ct}^*) E_p$.

In Eq. 2, $\overline{M} \Delta q^*$ represents the total water vapor flux in the domain that has the potential to generate precipitation. In moderate climates, q_{ct}^* is typically close to zero and can be neglected. However, in very hot climates, q_{ct}^* can reach values around 10^{-1}, making it nonnegligible (fig. S10, F to J). Moreover, not all condensation can transform to rain and reach the surface, as some may reevaporate when falls into a subsaturated or cloud-free layer. Thus, precipitation efficiency (E_p), the rate of net condensation to gross condensation in the whole air column, is included in the estimation. Equation 2 allows us to account for the impacts of entrainment and detrainment without explicitly constraining them.

In the cloud-resolving modeling, the convective updraft grid cells can be determined as the cloud condensation mixing ratio exceeding a threshold (e.g., 10^{-5}) and the vertical velocity being greater than a critical value (e.g., 1 m s^{-1}). Subsequently, the convective mass flux can be obtained from $M = \rho_a w_{up} \sigma_{up}$, in which ρ_a is the air density, w_{up} is the vertical velocity averaged over the whole updraft grid cells, and σ_{up} is the fraction area of the updraft grid cells over the entire domain.

Unfortunately, the released data by Seeley and Wordsworth (22) did not include the convective mass flux. Consequently, we diagnose M based on mass conservation and atmospheric energy balance. According to the principle of mass conservation, convective mass flux should have an equal value and be opposite to the subsidence mass flux, $\rho_a w_{sub}$, where w_{sub} (<0) is the averaged vertical velocity of the subsidence region. In the clear-sky subsidence region, it is the radiative cooling (Q_{rad}) and evaporating cooling (Q_{evap}) balanced by the dynamic heating (Q_{dyn}) of descending parcels by expansion, written as $Q_{dyn} = -(Q_{rad} + Q_{evap})$ (73, 74). Applying the weak temperature gradient approximation (75), Q_{dyn} in the subsidence region is approximately equal to $-\frac{w_{sub}}{c_p} \frac{\partial}{\partial z}(c_p T + gz)$, where c_p is the specific heat capacity of air at constant pressure, g is the surface gravity, and z is the height (76). Thus, the subsidence velocity can be approximated as

$$w_{sub} \cong \frac{-(Q_{rad} + Q_{evap})}{\frac{1}{c_p} \frac{\partial}{\partial z}(c_p T + gz)} = \frac{Q_{rad} + Q_{evap}}{\Gamma_d - \Gamma} \quad (12)$$

where Γ_d and Γ are the dry adiabatic lapse rate and environmental lapse rate, respectively. Consequently, the convective mass flux can be expressed as

$$M \cong -\rho_a w_{sub} \cong -\rho_a \frac{(Q_{rad} + Q_{evap})}{\Gamma_d - \Gamma} \quad (13)$$

Since the convective updraft region typically occupies a small fraction (~1%) of the entire domain, the subsidence area fraction is close to 1 (20). Therefore, we can calculate the convective mass flux profile using domain-mean radiative cooling, evaporating cooling, and lapse rate. This approach was verified in Jeevanjee (20) by comparing the convective mass flux profile with the $-\rho_a w_{sub}$ profile [see figure 3 in (20)]. In our study, we use the same method to diagnose the convective mass flux (M), and the vertically averaged $\overline{M}$ is calculated as $-\overline{\rho_a w_{sub}}$.

To quantitatively assess the effects of the three factors ($\overline{M}$, Δq^*, and E_p) on the trend of mean precipitation, we use a fractional type of Eq. 2, given by

$$\frac{\delta P}{P \delta T_s} \cong \frac{\delta \overline{M}}{\overline{M} \delta T_s} + \frac{\delta \Delta q^*}{\Delta q^* \delta T_s} + \frac{\delta E_p}{E_p \delta T_s} + res \quad (14)$$

The first three terms are the fractional changes of $\overline{M}$, Δq^*, and E_p, respectively, and the fourth term is the residual term (res), which comprises four small cross-sectional terms

$$\text{res} \equiv \frac{\delta\overline{M}\delta\Delta q^*}{\overline{M}\Delta q^*\delta T_s} + \frac{\delta E_p\delta\Delta q^*}{E_p\Delta q^*\delta T_s} + \frac{\delta E_p\delta\overline{M}}{E_p\overline{M}\delta T_s} + \frac{\delta E_p\delta\overline{M}\delta\Delta q^*}{P\delta T_s} \quad (15)$$

Dynamical constraint on precipitation in ExoCAM

The precipitation in the GCM ExoCAM consists of three components: deep convective precipitation (P_{deep}), shallow convective precipitation (P_{shallow}), and large-scale (nonconvective and stratiform) precipitation ($P_{\text{large}-\text{scale}}$). We use a similar equation to diagnose P_{deep} as that used in the cloud-resolving model by

$$P_{\text{deep}} \cong \overline{M_d}\Delta q^* E_{\text{pd}} = \overline{M_d}(q^*_{\text{LCL}} - q^*_{\text{ct}})E_{\text{pd}} \quad (16)$$

where $\overline{M_d}$ is the vertically averaged deep convective mass flux (including both dry air and water vapor) between the cloud base and cloud top, q^*_{LCL} is the saturated water vapor specific humidity at the LCL, q^*_{ct} is the saturated vapor specific humidity at the cloud top, and E_{pd} is the deep convective precipitation efficiency calculated as the ratio of net deep convective condensation to gross condensation in the deep convective scheme. Similar to Eq. 14, the fractional change of P_{deep} can be derived and the results are shown in fig. S5.

Similarly, the shallow convective precipitation (P_{shallow}) can be diagnosed by

$$P_{\text{shallow}} \cong W_{\text{shallow}}E_{\text{ps}} = \overline{M_s}\Delta q_{\text{eq}}E_{\text{ps}} \quad (17)$$

Here, W_{shallow} is the total shallow convective water flux, $\overline{M_s}$ is the averaged shallow convective mass flux, Δq_{eq} is the equivalent water vapor specific humidity difference between cloud base and cloud top for shallow convection, and E_{ps} is the shallow convective precipitation efficiency. Similar to Eq. 14, the fractional change of P_{shallow} can be expressed by

$$\frac{\delta P_{\text{shallow}}}{P_{\text{shallow}}\delta T_s} \cong \frac{\delta\overline{M_s}}{\overline{M_s}\delta T_s} + \frac{\delta\Delta q_{\text{eq}}}{\Delta q_{\text{eq}}\delta T_s} + \frac{\delta E_{\text{ps}}}{E_{\text{ps}}\delta T_s} + \text{res} \quad (18)$$

The residual term (res) includes four small cross-sectional parts: $\frac{\delta\overline{M_s}\delta q_{\text{eq}}}{\overline{M_s}\Delta q_{\text{eq}}\delta T_s}$, $\frac{\delta E_{\text{ps}}\delta\Delta q_{\text{eq}}}{E_{\text{ps}}\Delta q_{\text{eq}}\delta T_s}$, $\frac{\delta E_{\text{ps}}\delta\overline{M_s}}{E_{\text{ps}}M_s\delta T_s}$, and $\frac{\delta E_{\text{ps}}\delta\overline{M_s}\delta\Delta q_{\text{eq}}}{P_{\text{shallow}}\delta T_s}$. The values of W_{shallow} and $\overline{M_s}$ are available in the model output, but Δq_{eq} is not. Therefore, we calculate Δq_{eq} as $W_{\text{shallow}}/\overline{M_s}$, representing an equivalent value of water vapor specific humidity in shallow convection. E_{ps} is calculated as the ratio of net shallow convective condensation to the sum of gross condensation and the amount of liquid water detrained to neighboring grid cells in the shallow convective scheme. The inclusion of detrained liquid water is essential as liquid water may disperse into the environment within the shallow convective scheme (24). Note that shallow convection can initiate at any level within the model once the necessary condition is met (24), so the diagnosis is more complex than deep convection.

Large-scale precipitation ($P_{\text{large}-\text{scale}}$) is parameterized within each grid cell of the model. It is very difficult (if not impossible) to diagnose because many processes should be involved, such as the large-scale (resolvable) ascending in grid cells, the horizontal divergence of water vapor, and the detrained liquid water from convective columns. Rather than directly assessing $P_{\text{large}-\text{scale}}$, we address

its trend through analyzing the changes in the atmospheric overturning streamfunction and mid-latitude eddies (see fig. S6).

Supplementary Materials
This PDF file includes:
Figs. S1 to S10
Table S1

REFERENCES AND NOTES

1. S. Manabe, R. T. Wetherald, The effects of doubling the CO_2 concentration on the climate of a general circulation model. *J. Atmos. Sci.* **32**, 3–15 (1975).
2. I. M. Held, B. J. Soden, Robust responses of the hydrological cycle to global warming. *J. Climate* **19**, 5686–5699 (2006).
3. A. M. DeAngelis, X. Qu, M. D. Zelinka, A. Hall, An observational radiative constraint on hydrologic cycle intensification. *Nature* **528**, 249–253 (2015).
4. Douville, H., K. Raghavan, J. Renwick, R. P. Allan, P. A. Arias, M. Barlow, R. Cerezo-Mota, A. Cherchi, T. Y. Gan, J. Gergis, D. Jiang, A. Khan, W. Pokam Mba, D. Rosenfeld, J. Tierney, O. Zolina, Water Cycle Changes, in *Climate Change 2021: The Physical Science Basis. Contribution of Working Group I to the Sixth Assessment Report of the Intergovernmental Panel on Climate Change* (Cambridge Univ. Press, 2021), pp. 1055–1210.
5. M. R. Allen, W. J. Ingram, Constraints on future changes in climate and the hydrologic cycle. *Nature* **419**, 224–232 (2002).
6. R. T. Pierrehumbert, The hydrologic cycle in deep-time climate problems. *Nature* **419**, 191–198 (2002).
7. P. A. O'Gorman, T. Schneider, The hydrological cycle over a wide range of climates simulated with an idealized GCM. *J. Climate* **21**, 3815–3832 (2008).
8. P. A. O'Gorman, R. P. Allan, M. P. Byrne, M. Previdi, Energetic constraints on precipitation under climate change. *Surv. Geophys.* **33**, 585–608 (2012).
9. G. L. Stephens, J. Li, M. Wild, C. A. Clayson, N. Loeb, S. Kato, T. L'Ecuyer, P. W. Stackhouse, M. Lebsock, T. Andrews, An update on Earth's energy balance in light of the latest global observations. *Nat. Geosci.* **5**, 691–696 (2012).
10. N. Jeevanjee, D. M. Romps, Mean precipitation change from a deepening troposphere. *Proc. Natl. Acad. Sci. U.S.A.* **115**, 11465–11470 (2018).
11. A. G. Pendergrass, D. L. Hartmann, The atmospheric energy constraint on global-mean precipitation change. *J. Climate* **27**, 757–768 (2014).
12. D. D. B. Koll, T. W. Cronin, Earth's outgoing longwave radiation linear due to H_2O greenhouse effect. *Proc. Natl. Acad. Sci. U.S.A.* **115**, 10293–10298 (2018).
13. S. Nakajima, Y.-Y. Hayashi, Y. Abe, A study on the "runaway greenhouse effect" with a one-dimensional radiative–convective equilibrium model. *J. Atmos. Sci.* **49**, 2256–2266 (1992).
14. R. T. Pierrehumbert, *Principles of Planetary Climate* (Cambridge Univ. Press, ed. 1, 2010).
15. C. Goldblatt, T. D. Robinson, K. J. Zahnle, D. Crisp, Low simulated radiation limit for runaway greenhouse climates. *Nat. Geosci.* **6**, 661–667 (2013).
16. G. A. Vecchi, B. J. Soden, Global warming and the weakening of the tropical circulation. *J. Climate* **20**, 4316–4340 (2007).
17. G. Le Hir, Y. Donnadieu, Y. Goddéris, R. T. Pierrehumbert, G. P. Halverson, M. Macouin, A. Nédélec, G. Ramstein, The snowball Earth aftermath: Exploring the limits of continental weathering processes. *Earth Planet. Sci. Lett.* **277**, 453–463 (2009).
18. E. T. Wolf, O. B. Toon, The evolution of habitable climates under the brightening Sun. *J. Geophys. Res. Atmos.* **120**, 5775–5794 (2015).
19. A. K. Betts, Climate-convection feedbacks: Some further issues. *Clim. Change* **39**, 35–38 (1998).
20. N. Jeevanjee, Three rules for the decrease of tropical convection with global warming. *J Adv Model Earth Syst.* **14**, e2022MS003285 (2022).
21. S. Bony, B. Stevens, D. Coppin, T. Becker, K. A. Reed, A. Voigt, B. Medeiros, Thermodynamic control of anvil cloud amount. *Proc. Natl. Acad. Sci. U.S.A.* **113**, 8927–8932 (2016).
22. J. T. Seeley, R. D. Wordsworth, Episodic deluges in simulated hothouse climates. *Nature* **599**, 74–79 (2021).
23. M. Turbet, E. Bolmont, G. Chaverot, D. Ehrenreich, J. Leconte, E. Marcq, Day–night cloud asymmetry prevents early oceans on Venus but not on Earth. *Nature* **598**, 276–280 (2021).
24. R. B. Neale, J. Richter, A. Conley, S. Park, P. Lauritzen, A. Gettelman, D. Williamson, P. Rasch, S. Vavrus, M. Taylor, others, Description of the NCAR Community Atmosphere Model (CAM 4.0), NCAR Tech. Note, TN–485. 212 (2010).
25. D. Chen, A. Dai, Precipitation characteristics in the Community Atmosphere Model and their dependence on model physics and resolution. *J. Adv. Model. Earth Syst.* **11**, 2352–2374 (2019).

26. A. L. Shields, V. S. Meadows, C. M. Bitz, R. T. Pierrehumbert, M. M. Joshi, T. D. Robinson, The effect of host star spectral energy distribution and ice-albedo feedback on the climate of extrasolar planets. *Astrobiology* **13**, 715–739 (2013).

27. J. K. Eager-Nash, D. J. Reichelt, N. J. Mayne, F. Hugo Lambert, D. E. Sergeev, R. J. Ridgway, J. Manners, I. A. Boutle, T. M. Lenton, K. Kohary, Implications of different stellar spectra for the climate of tidally locked Earth-like planets. *A&A.* **639**, A99 (2020).

28. J. Yang, G. Boué, D. C. Fabrycky, D. S. Abbot, Strong dependence of the inner edge of the habitable zone on planetary rotation rate. *ApJ.* **787**, L2 (2014).

29. J. Salameh, M. Popp, J. Marotzke, The role of sea-ice albedo in the climate of slowly rotating aquaplanets. *Climate Dynam.* **50**, 2395–2410 (2018).

30. M. J. Way, A. D. Del Genio, I. Aleinov, T. L. Clune, M. Kelley, N. Y. Kiang, Climates of warm Earth-like planets. I. 3D model simulations. *ApJS.* **239**, 24 (2018).

31. C. J. Poulsen, C. Tabor, J. D. White, Long-term climate forcing by atmospheric oxygen concentrations. *Science* **348**, 1238–1241 (2015).

32. J. Xiong, J. Yang, J. Liu, Smaller sensitivity of precipitation to surface temperature under massive atmospheres. *Geophys. Res. Lett.* **49**, e2022GL099599 (2022).

33. S. I. Thomson, G. K. Vallis, The effects of gravity on the climate and circulation of a terrestrial planet. *Q.J.R. Meteorol. Soc.* **145**, 2627–2640 (2019).

34. J. Liu, J. Yang, Y. Zhang, Z. Tan, Convection and clouds under different planetary gravities simulated by a small-domain cloud-resolving model. *ApJ.* **944**, 45 (2023).

35. R. Caballero, M. Huber, State-dependent climate sensitivity in past warm climates and its implications for future climate projections. *Proc. Natl. Acad. Sci. U.S.A.* **110**, 14162–14167 (2013).

36. D. M. Romps, Climate sensitivity and the direct effect of carbon dioxide in a limited-area cloud-resolving model. *J. Climate* **33**, 3413–3429 (2020).

37. J. E. Lovelock, M. Whitfield, Life span of the biosphere. *Nature* **296**, 561–563 (1982).

38. K. Caldeira, J. F. Kasting, The life span of the biosphere revisited. *Nature* **360**, 721–723 (1992).

39. J. Yang, N. B. Cowan, D. S. Abbot, Stabilizing cloud feedback dramatically expands the habitable zone of tidally locked planets. *ApJ.* **771**, L45 (2013).

40. J. F. Kasting, *How to Find a Habitable Planet* (Princeton Univ. Press, 2010).

41. J. C. G. Walker, P. B. Hays, J. F. Kasting, A negative feedback mechanism for the long-term stabilization of Earth's surface temperature. *J. Geophys. Res.* **86**, 9776–9782 (1981).

42. P. F. Hoffman, A. J. Kaufman, G. P. Halverson, D. P. Schrag, A neoproterozoic snowball earth. *Science* **281**, 1342–1346 (1998).

43. K. Loftus, R. D. Wordsworth, The physics of falling raindrops in diverse planetary atmospheres. *JGR Planets.* **126**, e2020JE006653 (2021).

44. X. Song, D. S. Abbot, J. Yang, Critical role of vertical radiative cooling contrast in triggering episodic deluges in small-domain hothouse climates. arXiv:2307.01219 (2023).

45. G. Dagan, J. T. Seeley, N. Steiger, Convection and Convective-Organization in Hothouse Climates. *J Adv Model Earth Syst* **15**, e2023MS003765 (2023).

46. F. E. Spaulding-Astudillo, J. L. Mitchell, The emergence of relaxation-oscillator convection on Earth and Titan. *arXiv.* **2306**, 03219 (2023).

47. F. R. Robe, K. A. Emanuel, Moist Convective Scaling: Some Inferences from Three-Dimensional Cloud Ensemble Simulations. *J. Atmos. Sci.* **53**, 3265–3275 (1996).

48. E. T. Wolf, J. Haqq-Misra, O. B. Toon, Evaluating climate sensitivity to CO_2 across Earth's history. *JGR Atmospheres.* **123**, 11861–11874 (2018).

49. Y. Zhang, J. Bloch-Johnson, D. M. Romps, D. S. Abbot, Evolving CO_2 rather than SST leads to a factor of ten decrease in GCM convergence time. *J Adv Model Earth Syst* **13**, e2021MS002505 (2021).

50. E. T. Wolf, O. B. Toon, Hospitable Archean climates simulated by a general circulation model. *Astrobiology* **13**, 656–673 (2013).

51. G. J. Zhang, N. A. McFarlane, Sensitivity of climate simulations to the parameterization of cumulus convection in the Canadian climate centre general circulation model. *Atmosphere-Ocean.* **33**, 407–446 (1995).

52. J. H. Richter, P. J. Rasch, Effects of convective momentum transport on the atmospheric circulation in the Community Atmosphere Model, Version 3. *J. Climate* **21**, 1487–1499 (2008).

53. D. J. Raymond, A. M. Blyth, A Stochastic mixing model for nonprecipitating cumulus clouds. *J. Atmos. Sci.* **43**, 2708–2718 (1986).

54. D. J. Raymond, A. M. Blyth, Extension of the stochastic mixing model to cumulonimbus clouds. *J. Atmos. Sci.* **49**, 1968–1983 (1992).

55. J. J. Hack, Parameterization of moist convection in the National Center for Atmospheric Research community climate model (CCM2). *J. Geophys. Res.* **99**, 5551–5568 (1994).

56. M. J. Way, N. Georgakarakos, Effects of variable eccentricity on the climate of an Earth-like world. *ApJ.* **835**, L1 (2017).

57. W. D. Collins, P. J. Rasch, B. A. Boville, J. J. Hack, J. R. McCaa, D. L. Williamson, B. P. Briegleb, C. M. Bitz, S.-J. Lin, M. Zhang, The formulation and atmospheric simulation of the Community Atmosphere Model Version 3 (CAM3). *J. Climate* **19**, 2144–2161 (2006).

58. W. D. Collins, C. M. Bitz, M. L. Blackmon, G. B. Bonan, C. S. Bretherton, J. A. Carton, P. Chang, S. C. Doney, J. J. Hack, T. B. Henderson, J. T. Kiehl, W. G. Large, D. S. McKenna, B. D. Santer, R. D. Smith, The Community Climate System Model Version 3 (CCSM3). *J. Climate* **19**, 2122–2143 (2006).

59. Z. X. Li, S. V. Bogdanova, A. S. Collins, A. Davidson, B. De Waele, R. E. Ernst, I. C. W. Fitzsimons, R. A. Fuck, D. P. Gladkochub, J. Jacobs, K. E. Karlstrom, S. Lu, L. M. Natapov, V. Pease, S. A. Pisarevsky, K. Thrane, V. Vernikovsky, Assembly, configuration, and break-up history of Rodinia: A synthesis. *Precambrian Res.* **160**, 179–210 (2008).

60. G. Le Hir, G. Ramstein, Y. Donnadieu, R. T. Pierrehumbert, Investigating plausible mechanisms to trigger a deglaciation from a hard snowball Earth. *C. R. Geosci.* **339**, 274–287 (2007).

61. Y. Hu, J. Yang, F. Ding, W. R. Peltier, Model-dependence of the CO_2 threshold for melting the hard Snowball Earth. *Clim. Past.* **7**, 17–25 (2011).

62. D. M. Romps, The dry-entropy budget of a moist atmosphere. *J. Atmos. Sci.* **65**, 3779–3799 (2008).

63. F. Guichard, F. Couvreux, A short review of numerical cloud-resolving models. *Tellus A: Dynamic Meteorol. Oceanog.* **69**, 1373578 (2022).

64. R. Wordsworth, Y. Kalugina, S. Lokshtanov, A. Vigasin, B. Ehlmann, J. Head, C. Sanders, H. Wang, Transient reducing greenhouse warming on early Mars. *Geophys. Res. Lett.* **44**, 665–671 (2017).

65. M. F. Khairoutdinov, D. A. Randall, Cloud resolving modeling of the ARM Summer 1997 IOP: Model formulation, results, uncertainties, and sensitivities. *J. Atmos. Sci.* **60**, 607–625 (2003).

66. S. L. Grimm, K. Heng, HELIOS-K: An ultrafast, open-source opacity calculator for radiative transfer. *ApJ.* **808**, 182 (2015).

67. NIST Standard Reference Database Number 69 (2023); https://doi.org/10.18434/T4D303.

68. J. F. Kasting, Runaway and moist greenhouse atmospheres and the evolution of Earth and Venus. *Icarus.* **74**, 472–494 (1988).

69. The Engineering ToolBox, moist air-water vapor and saturation pressure (2004); https://engineeringtoolbox.com/water-vapor-saturation-pressure-air-d_689.html.

70. D. L. Hartmann, K. Larson, An important constraint on tropical cloud-climate feedback: Tropical cloud-climate feedback. *Geophys. Res. Lett.* **29**, 121–124 (2002).

71. T. Schneider, P. A. O'Gorman, X. J. Levine, Water vapor and the dynamics of climate changes. *Rev. Geophys.* **48**, RG3001 (2010).

72. D. M. Romps, An analytical model for tropical relative humidity. *J. Climate* **27**, 7432–7449 (2014).

73. A. M. Jenney, D. A. Randall, M. D. Branson, Understanding the response of tropical ascent to warming using an energy balance framework. *J. Adv. Model. Earth Syst.* **12**, e2020MS002056 (2020).

74. T. R. Knutson, S. Manabe, Time-mean response over the tropical Pacific to increased CO_2 in a coupled ocean-atmosphere model. *J. Climate* **8**, 2181–2199 (1995).

75. J. G. Charney, A note on large-scale motions in the tropics. *J. Atmos. Sci.* **20**, 607–609 (1963).

76. D. M. Romps, Theory of tropical moist convection in *Fundamental Aspects of Turbulent Flows in Climate Dynamics* (Oxford University Press, 2020), pp. 1–45.